Acta Materialia 221 (2021) 117403

Contents lists available at ScienceDirect

Acta Materialia

journal homepage: www.elsevier.com/locate/actamat

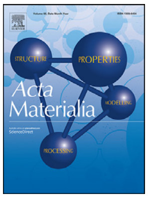

Full length article

Energy-storage-efficient $0.9Pb(Mg_{1/3}Nb_{2/3})O_3$–$0.1PbTiO_3$ thick films integrated directly onto stainless steel

Matej Sadl[a,b], Oana Condurache[a,b], Andreja Bencan[a,b], Mirela Dragomir[a], Uros Prah[a,b], Barbara Malic[a,b], Marco Deluca[c], Udo Eckstein[d], Daniel Hausmann[e], Neamul H. Khansur[d], Kyle G. Webber[d], Hana Ursic[a,b,*]

[a] Electronic Ceramics Department, Jožef Stefan Institute, Jamova cesta 39, 1000 Ljubljana, Slovenia
[b] Jožef Stefan International Postgraduate School, Jamova cesta 39, 1000 Ljubljana, Slovenia
[c] Materials Center Leoben Forschung GmbH (MCL), Roseggerstrasse 12, 8700 Leoben, Austria
[d] Department of Materials Science and Engineering, Friedrich-Alexander-Universität Erlangen-Nürnberg (FAU), 91058 Erlangen, Germany
[e] Institute of General Material Properties, Friedrich-Alexander-Universität Erlangen-Nürnberg (FAU), 91058 Erlangen, Germany

ARTICLE INFO

Article history:
Received 3 March 2021
Revised 20 September 2021
Accepted 12 October 2021
Available online 18 October 2021

Keywords:
Thick film
Aerosol deposition
Low-temperature processing
Energy storage
PMN–PT
Relaxor-ferroelectric
Stainless steel

ABSTRACT

The integration of functional ceramics with metals remains challenging due to the thermally activated processes and the incompatibilities that arise during the high-temperature ceramic sintering process. In order to overcome this, low-temperature processing methods can be employed. In this work, dense $0.9Pb(Mg_{1/3}Nb_{2/3})O_3$–$0.1PbTiO_3$ thick films were deposited on low-cost, stainless-steel substrates at room temperature using an aerosol-deposition method. The key material parameters for a successful aerosol deposition of the powder were identified and used in the process, which resulted in homogeneous 15-µm-thick films. The as-deposited films can withstand electric fields of 900 $kV\cdot cm^{-1}$ and exhibit promising room-temperature energy-storage properties: the recoverable energy density reaches 7.0 $J\cdot cm^{-3}$ with an energy-storage efficiency of ~70%. A post-deposition stress relaxation by annealing at 500°C further improves the recoverable energy density, leading to 9.8 $J\cdot cm^{-3}$ at 900 $kV\cdot cm^{-1}$ with an energy-storage efficiency of ~80%. The energy-storage performance exhibits excellent temperature stability up to 200°C and an electric-field cycling stability up to 16 million cycles. The low-temperature integration of energy-storage-efficient thick films onto stainless steel opens up possibilities for numerous new, pulsed-power and power-conditioning electronic applications.

1. Introduction

Ceramic dielectric capacitors can absorb and release large voltage or current pulses in a short timeframe (i.e., between µs and ms), making them promising for energy-storage devices in pulsed-power and power-conditioning electronic applications. These can be found in medical equipment, transportation, avionics, energy systems such as photovoltaics and other commercial systems [1–3]. Ceramic dielectric capacitors, however, possess energy-density values some orders of magnitude lower than supercapacitors or batteries. Increasing the energy density of ceramic dielectric capacitors might thus open up possibilities for new applications in which they could – at least partly – replace long-term, energy-storage devices. Dense materials in the form of films with thicknesses around or above 1 µm show the most promising energy-storage properties so far [4].

The materials used for capacitors in energy-storage applications need to operate under demanding conditions such as high electric fields, a broad temperature range and they need to endure repetitive electric-field cycling. Ceramic thick films based on relaxor-ferroelectrics $(1-x)Pb(Mg_{1/3}Nb_{2/3})O_3$–$xPbTiO_3$ (PMN–100xPT) cope well with all these requirements. Among them, PMN–10PT is interesting for such applications as it exhibits small hysteresis losses, which is evident from the slim electric polarization (P) vs. electric field (E) hysteresis loops [5]. The requirements for a large dielectric-breakdown strength of ceramics can be achieved by increasing the material's density and reducing the thickness of the capacitor. As such, dense PMN–10PT thick films have excellent possibilities to achieve a high energy-storage performance in layered ceramic dielectric capacitors.

---

[*] Corresponding author.
E-mail address: hana.ursic@ijs.si (H. Ursic).

https://doi.org/10.1016/j.actamat.2021.117403
1359-6454/

Conventional thick-film deposition methods, such as screen-printing, tape-casting or electrophoretic deposition, are followed by a high-temperature annealing (often above 1000 °C) to densify the deposited films [6]. However, annealing at such high temperatures imposes many drawbacks. High annealing temperatures increase the production costs and promote the evaporation of volatile components, which can significantly deteriorate the chemical composition of functional layers. Furthermore, annealing at high temperatures restricts the use of substrate materials with a low oxidation resistance and a low melting point, such as metals. This limits the integration possibilities of ceramic layers on metal substrates, which is especially important when designing new applications [6]. In order to overcome these shortcomings, aerosol deposition (AD) can be used. AD is a spray-coating method for preparing dense, several-μm-thick films at room temperature. The deposition mechanism is based on the collision of high-speed particles with the substrate's surface and the densification occurs as a consequence of the high kinetic energies involved [7,8].

Stainless steel is an iron-based alloy containing chromium, which makes it durable and resistant to corrosion and wear. It is a low-cost material that is used in various applications, e.g., in buildings and monuments, manufacturing, medicine, power stations, vehicles, spacecraft and many other appliances and consumer products [9–11]. The integration of functional layers directly onto stainless-steel surfaces is a very important scientific and technological challenge with enormous potential for applications. The processing and characterization of piezoelectric $Pb(Zr,Ti)O_3$-based [12–16] and lead-free [17–19] thick films on stainless steel have been widely reported; however, no reports of energy-storage-efficient PMN-based thick films on stainless steel are available.

In this work, PMN–10PT thick films were directly deposited by AD on stainless-steel substrates without any additional intermediate layers (electrodes or barrier layers). For the successful deposition of films by AD, the powder properties need to be optimized. According to the literature [8], powders with a particle size ranging between 0.2 μm and 2 μm can be successfully deposited by AD. However, the deposition is not just particle-size dependent; it also depends on the particles' shape, state of agglomeration, hardness, average crystallite size, etc. [8,20,21]. Milling and thermal pre-treatment of the powder are thus crucial for an efficient film deposition. This work investigates the influence of PMN–10PT powder properties on the deposition rate. Four different PMN–10PT powders were prepared and deposited on the stainless-steel substrates. The optimum powder resulted in dense films that were a few μm thick.

According to reports in the literature, the impact of ceramic particles during the AD process creates internal stresses in the deposited material [19,22,23]. The post-deposition annealing of prepared films will induce an increase in the size of the crystallites [24] and the relaxation of internal stresses [19,25], which can lead to improved functional properties. Therefore, in the second part of this work, the influence of thermal annealing on the structural, microstructural and energy-storage properties of PMN–10PT thick films on stainless-steel substrates is discussed.

2. Experimental procedure

For the synthesis of the PMN–10PT ceramic powder, PbO (99.9%, Aldrich), MgO (99.95%, Alfa Aesar), TiO_2 (99.8%, Alfa Aesar) and Nb_2O_5 (99.9%, Aldrich) were employed. Two sets of oxide mixtures corresponding to the stoichiometry of $Pb(Mg_{1/3}Nb_{2/3})O_3$ and $PbTiO_3$ were homogenized separately. The PT powder mixture was calcined at 750°C for 2 h and additionally milled in order to obtain crystalline PT seeds. It was reported that such PT seeds facilitate faster kinetics of the PMN–10PT perovskite-phase formation and shorten the high-energy milling time [26]. PT and PMN powder mixtures were homogenized with a stoichiometry of $0.9Pb(Mg_{1/3}Nb_{2/3})O_3–0.1PbTiO_3$. This mixture was reacted by mechanochemical-activation-assisted synthesis, also known as high-energy milling, after which the synthesized powder was milled. All homogenization and milling processes were carried out in a planetary ball mill (PM 400, Retsch, Germany) at 200 min^{-1} for 2 h, in isopropanol, using yttria-stabilized zirconia (YSZ) milling balls with diameters of 3 mm. The high-energy milling involved the same planetary ball mill, but for 36 h at 300 min^{-1} in a tungsten-carbide milling vial with a volume of 250 cm^3, filled with 10 tungsten-carbide milling balls having diameters of 20 mm. In addition to the thick films, the PMN–10PT bulk ceramic pellets with an average grain size of 4.4 μm were prepared via mechanochemical-activation-assisted synthesis and sintering at 1200°C for 2 h, as previously reported in ref. [27].

The as-synthesized PMN–10PT powder was further processed to obtain four powder modifications, which were used in the AD process. The first powder, here referred to as the non-treated powder (NT), did not receive any post-synthesis treatment. The remaining three powders were thermally treated at 900°C for 1 h. The second powder (H) was subjected only to the heat treatment, while the third (HM30) and fourth (HM60) powders were subjected to an additional ball milling for 30 min and 60 min, respectively. The milling conditions were similar to those used in the previous steps, i.e., milling at 200 min^{-1} in isopropanol using YSZ milling balls with diameters of 3 mm. Prior to the AD, the powders were sieved through a 200-μm mesh and vacuum dried for 12 h at 100°C and at 10 mbar.

The AD equipment was provided by InVerTec, Germany. Commercial stainless steel (SS, no. 304, American Iron and Steel Institute) with a bright, polished surface (A480: No. 8, American Society for Testing and Materials) and dimensions 15 mm × 15 mm × 0.8 mm was used as the substrate. The process parameters during the AD, reported elsewhere [28], were kept the same for the deposition of all four powders. After the AD, the samples were cleaned with ethanol and annealed at 500°C for 1 h using 2 $K\cdot min^{-1}$ heating and cooling rates in order to release the internal stresses developed in the material during deposition.

The X-ray diffraction (XRD) analysis was performed with a high-resolution diffractometer (X'Pert PRO, PANalytical, Netherlands) using Cu–Kα_1 radiation. Diffraction patterns were recorded in the Bragg–Brentano geometry using a 100-channel X'Celerator detector in a 2θ range of 10°–120° with a step of 0.017° and an integration time of 100 s per step. The Topas R package (version 2.1, Bruker AXS GmbH, Germany) was employed for the Rietveld refinement and the Fundamental Parameters Approach (FPA) was used for the line-profile fitting of all the samples [29]. The FPA uses the geometrical properties of the diffraction experiment to build up the instrumental line width from first principles. It thus allows an explicit determination of the sample-dependent line-broadening contributions to the peak profile, which are dominated by the microstrain and broadening due to decrease in the crystallite size [30]. The microstructure effects were modeled using the Double-Voigt approach [31]. The volume-weighted mean crystallite size was calculated based on the integral breath method incorporated in the Topas software. The residual stress analyses of the films in the Bragg–Brentano geometry were performed with a high-resolution XRD diffractometer (Bruker D8 Advance, Bruker AXS GmbH, Germany) using Cu–Kα_1 radiation equipped with a Eulerian cradle.

Particle size analyses were performed using a light-scattering laser granulometer (S3500, Microtrac, USA) with isopropanol (IPA) as a medium. Prior to the measurement the powder in the liquid medium was placed in an ultrasonic bath (PRO 50, ASonic, China) for a few minutes in order to break the agglomerates.

Scanning electron microscopy (SEM) analyses were performed with a field-emission scanning electron microscope (FE-SEM, JSM-7600F, JEOL, Japan) equipped with an energy-dispersive X-ray spectrometer (EDXS, Inca Oxford 350 EDS SSD, Oxford Instruments, UK). For the SEM analyses, the powders were deposited on carbon tape. In the case of the thick films, plain surfaces and polished cross-sections were analysed. For the cross-sectional analyses, the samples were cut, mounted in epoxy resin, ground and fine-polished using a colloidal silica suspension. Prior to the SEM analyses, all the samples were coated with a 3-nm-thick carbon layer using a Precision Etching and Coating System (PECS 682, Gatan, USA).

The porosity of thick films was estimated from SEM cross-sectional images using the Image Tool software (UTHSCSA Image Tool Version 3.00. 2002, [32]). Also the size analyses of the powder particles were based on SEM images with the Image Tool software and measuring more than 150 particles. The data are presented as a number particle size distribution and the particle size is expressed as Feret's diameter [33].

The transmission electron microscopy (TEM), including selected-area electron diffraction (SAED), of the powders dispersed on a grid and the thick films in cross-section were performed using JEM 2100 and JEM 2010F (JEOL, Japan) microscopes, respectively. Prior to the analyses, the thick-film samples were cut, ground, dimpled and finally Ar-ion milled (PIPS 691, Gatan, USA). The SAED patterns were indexed according to the cubic perovskite structure (JCPDS 81-0861, $Pm\bar{3}m$ space group).

Raman measurements of the thick films were performed with a single spectrograph apparatus (LabRAM 300, Horiba Jobin Yvon, France), using an excitation wavelength of 532 nm. The spectra were collected in the backscattered geometry with an edge filter (cut-off: 80 cm^{-1}), 1800 $\mathrm{gr \cdot mm}^{-1}$ grating, slit size of 100 µm and a charge-coupled-device camera. The laser beam spot had a diameter of ~1 µm on the specimen's surface.

The film thickness was evaluated from the step height of the line profiles measured with a contact profilometer (DektakXT, Bruker, USA). A quadratic polynomial was used for the curvature removal on the line profiles. For each powder, the deposition rate (DR) was calculated from the film thickness (h), film width (w), sweep speed (v) and number of scans (N), according to the following Eq. (1):

$$DR = \frac{h \cdot w \cdot v}{N} \tag{1}$$

For the electrical measurements, the bulk ceramic pellets were cut to a thickness of ~200 µm and polished, while in the case of the thick films no additional preparation was needed. In both cases, the surfaces were coated with Au electrodes using a RF-magnetron sputtering machine (5 Pascal, Italy). The diameters of the electrodes sputtered on the thick-film and ceramic surfaces were 1.5 mm and 5 mm, respectively. The unipolar polarization–electric field (P–E) hysteresis loops of the films and ceramics were measured using an aixACCT TF analyzer 2000 (aixACCT Systems GmbH, Germany) by applying a single sinusoidal waveform with a frequency of 100 Hz. For the P–E loops that were measured at temperatures ranging from 0°C to 200°C and during room-temperature repetitive electric-field cycling an electric field of 500 $\mathrm{kV \cdot cm}^{-1}$ was applied.

3. Results and discussion

3.1. Influence of the powder properties on the AD rate

Initially, the influence of the powder properties on the aerosol-deposition rate was studied. The morphology, state of agglomeration and particle size of all four PMN–10PT powders were investigated using laser granulometry, SEM and TEM. The laser granulometric analyses are shown in Supplementary material S1. The measurements made in isopropanol (IPA) revealed multimodal size distributions and a broad particle size range in all the powders, i.e., between 100 nm and a few tens of micrometers, indicating the formation of agglomerates, presumably partially related to the IPA liquid medium used during the measurements. Note also that the sub-100-nm particles were not detected by laser granulometry, due to the detection limit of the device [34]. On the other hand, the particle size analyses by SEM (Fig. 1) revealed non-agglomerated particles with sizes below 500 nm.

According to data from the SEM analyses (Fig. 1d, h, l, p), the non-treated (NT) powder consists of the smallest particles. These particles are, according to the SEM and TEM, irregularly shaped and their size range is between 20 nm and 120 nm, with a median particle size (d_{50}) of 50 nm (Fig. 1d). Such small particles tend to reduce their surface energy by assembling into agglomerates larger than 200 nm, as observed in Fig. 1b and c.

The thermal treatment completely modifies the powder properties, since the early stages of interparticle sintering occur due to sufficient thermal energy being available. The H powder consists mainly of large, round-like particles with smooth surfaces. According to the particle size distribution determined from the SEM micrographs (Fig. 1h), the size of these particles ranges between 150 nm and 450 nm, with a d_{50} of 250 nm.

Milling influences both the particle size and shape. In comparison to the H powder, the milled HM30 powder contains smaller particles with sizes between 100 nm and 400 nm, and a d_{50} of 220 nm (Fig. 1l). Due to milling, the particles are also more irregularly shaped in comparison to the round-like particles of the H powder.

Further milling leads to the formation of more irregularly shaped particles with fresh surfaces and higher specific surface energies [35]. These particles tend to reduce their surface energy by assembling into large agglomerates, some of them exceeding 2000 nm (Fig. 1m). According to the particle size distribution determined from the SEM micrographs (Fig. 1p), the size of the HM60 powder particles typically ranges between 50 nm and 400 nm, with a d_{50} of 200 nm. Despite progressive milling, these few-hundred-nm-sized particles (Fig. 1o) can be identified as single crystalline particles according to the SAED analysis (Supplementary material S2). Furthermore, in all three heat-treated powders, a few examples of particles with sizes around or below 100 nm were observed with the TEM (Fig. 1g, k and o).

X-ray diffraction analyses (XRD) were performed on all four PMN–10PT powders (Fig. 2). All the powders were indexed to the perovskite structure with the $Pm\bar{3}m$ space group (JCPDS 81-0861). No secondary phases were detected. The XRD patterns reveal a substantial peak broadening of the NT powder compared to other samples. Such broadening is evidence of a reduced crystallite size and/or microstrain. These XRD patterns were examined in detail using Rietveld refinements and the results are shown in Fig. 2c. The smallest average crystallite size of 21 nm ± 1 nm and the largest microstrain of $15.4 \cdot 10^{-4} \pm 0.8 \cdot 10^{-4}$ was found in the NT powder that was high-energy milled, but not thermally treated afterwards. In the other three powders that were exposed to a thermal treatment, the average crystallite size increased to ~190 nm and the microstrain decreased below $2.0 \cdot 10^{-4}$. Note that the crystallite size of the heat-treated powders is comparable to the particle size determined by the SEM analysis (Fig. 1), where d_{50} is slightly above 200 nm. These particles are mainly single crystalline, which was confirmed by the SAED analyses (Supplementary material S2).

Finally, all four powders were deposited on stainless-steel (SS) substrates under similar conditions. Fig. 3a shows photographs of the deposited thick films and their surface line scans, while the SEM images of the films in cross-section are shown in Fig. 3b. The

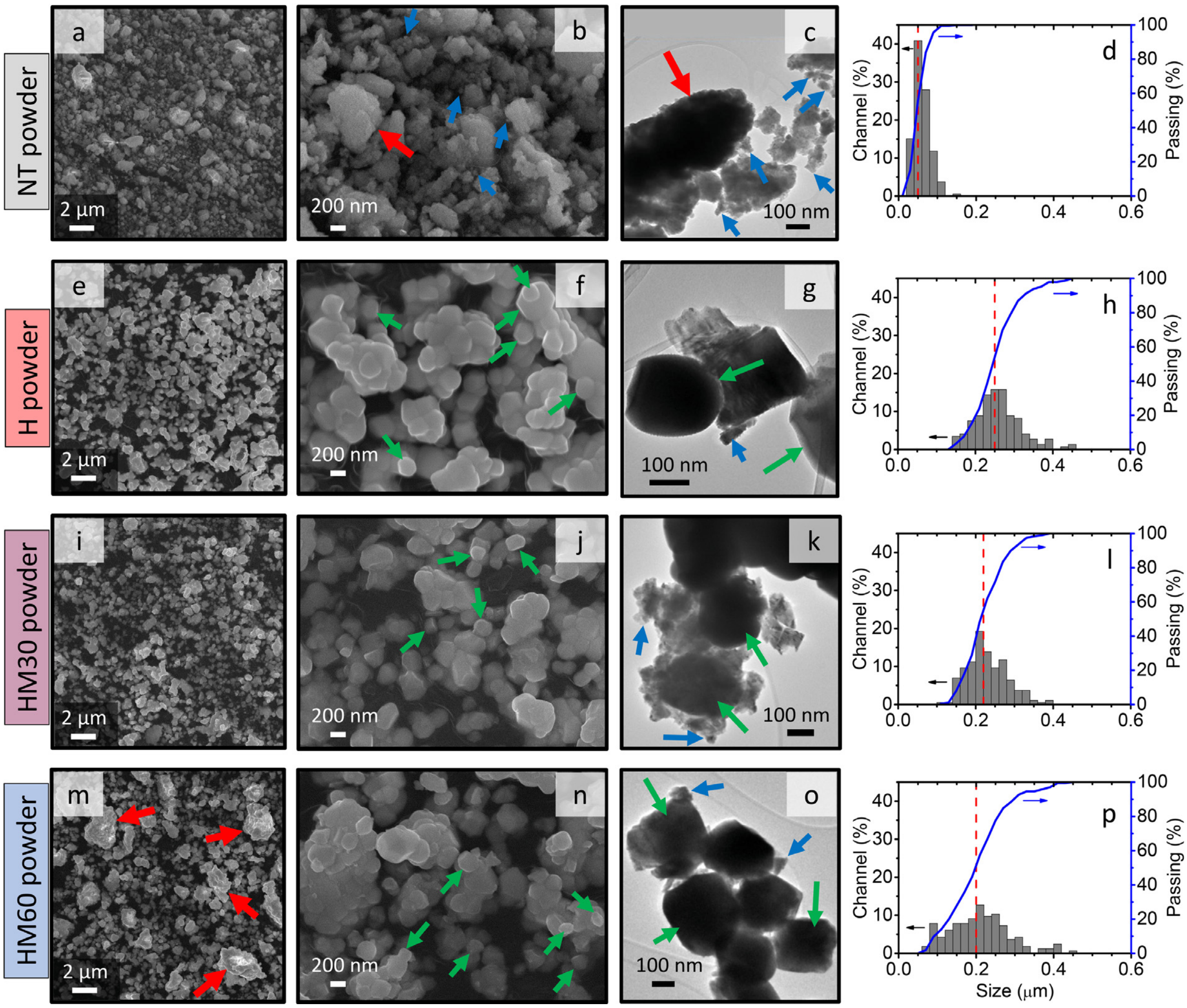

Fig. 1. SEM micrographs (1st and 2nd columns), bright-field TEM micrographs (3rd column) and particle size distribution from SEM micrographs (4th column) of the NT powder (1st row), H powder (2nd row), HM30 powder (3rd row) and HM60 powder (4th row). Blue and green arrows mark clearly visible particles of a few tens and a few hundreds of nm in size, respectively. Red arrows mark agglomerates. Note the different scales of individual panels. The vertical red dashed lines represent d_{50}. (For interpretation of the references to colour in this figure legend, the reader is referred to the web version of this article.)

deposition of the NT powder was not successful. There was only a build-up of a pile of loose powder, which was easily wiped off. Importantly, the NT powder was found to contain relatively small particles in the range of tens of nm. According to the literature, such small particles ($<$ 100 nm) are either deflected during the AD process by bow shocks before reaching the substrate or they elastically bounce off the substrate. Consequently, these particles do not plastically deform or fracture and, therefore, a room-temperature impact consolidation mechanism is not reached [8].

Both the H and HM30 powders resulted in consolidated films with homogeneous thicknesses over the whole deposition area (Fig. 3a). The films' surface profiles indicate that the edge of each film is slightly thicker. A reason for that could be the higher deposition rate that might occur locally due to the mask used for the film edges [36]. The calculated deposition rates of the H and HM30 powders, presented in Fig. 3c, reach 0.15 $mm^3 \cdot min^{-1}$ and 0.27 $mm^3 \cdot min^{-1}$, respectively. Such high deposition rates are typically achieved with the AD method [37,38]. The additional heating of the powder provided sufficiently large particles with a d_{50} of 250 nm, which enabled their successful deposition. Further milling slightly reduced the d_{50} to 220 nm, which correlates with the increasing deposition rate of the HM30 powder. This is in agreement with other reports [39,40], where it was explained that smaller particles can be more easily dispersed in a turbulent gas flow than larger particles. Thus, milling of the powder increases the aerosol concentration in the aerosol-generation process, leading to a higher deposition rate.

With a longer milling time, the HM60 powder resulted in an unsuccessful and uncontrolled film deposition (Fig. 3). After the AD, piles of loose powder were easily wiped off and only a partially covered deposition area remained. The result indicates a dual nature of the HM60 powder. Besides the particles that have a potential to form very dense films, a fraction of the powder is depositing without consolidation. This powder fraction is most likely represented by the large agglomerates that are identified in Fig. 1m. It is known that the presence of agglomerates can disturb successful film formation due to the different impact behaviour of agglomerates in comparison to single-grain particles [8]. During the AD, agglomerates are most likely to accumulate on the surface of the nozzle and pipes until a critical amount is reached and the agglomerates are released in the aerosol flow. Because of the repetitive process, the concentration of agglomerates in the aerosol varies over time, resulting in an inhomogeneous film thickness.

In the first part of our study, it was shown how crucial the powder preparation is for a successful aerosol deposition. A combination of heating and subsequent milling proved to be impor-

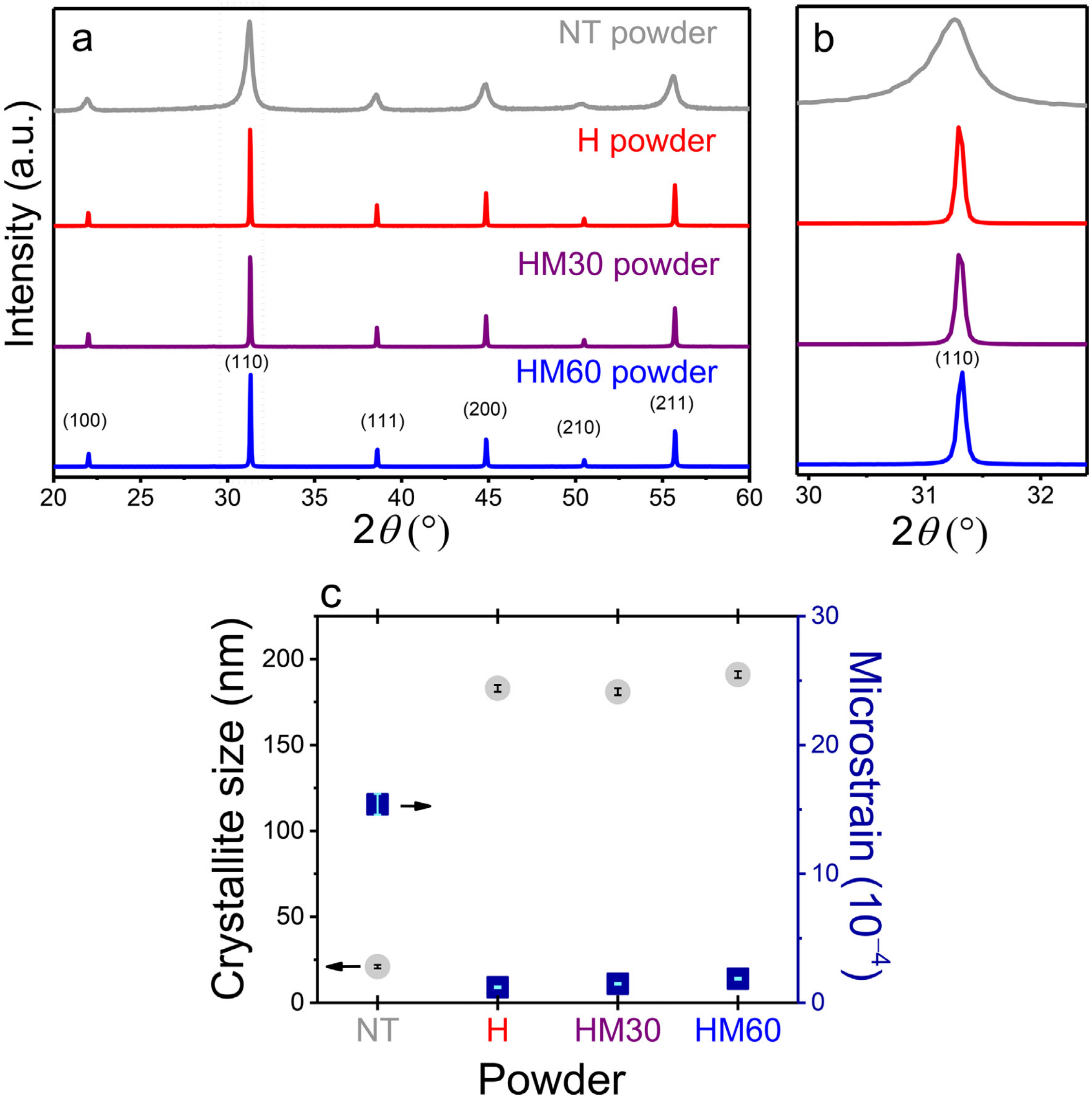

Fig. 2. (a) Zoom-in XRD patterns in the 2θ range 20–60° for powders used in the AD. All the peaks were indexed to a cubic perovskite structure. (b) Enlarged view of (110) cubic reflection. (c) The corresponding crystallite size (grey circles) and microstrain (blue squares) evaluated by Rietveld refinement. (For interpretation of the references to colour in this figure legend, the reader is referred to the web version of this article.)

tant for obtaining a PMN–10PT powder with an optimized particle size, which enables the formation of dense and homogeneous thick films at increased deposition rates. The most successful deposition was achieved with the HM30 powder. Therefore, all the thick films used in subsequent analyses were prepared from this powder. In the next part of this study, the influence of thermal annealing at 500°C on the structural, microstructural and functional properties of the thick films prepared from the HM30 powder on low-cost stainless steel is discussed.

3.2. Influence of annealing on the structural, microstructural, and energy-storage properties of AD films

Next, the influence of annealing on the structural, microstructural, and energy-storage properties of AD thick films is studied. The films are denoted as “as-deposited” or “annealed”. The XRD patterns of the as-deposited and annealed thick films are shown in Fig. 4a. The XRD pattern of the starting HM30 powder is added for comparison. All the samples were indexed to the perovskite structure with the $Pm\bar{3}m$ space group (JCPDS 81-0861). No secondary phases were detected and no peak shift could be observed. In comparison with the HM30 powder, the as-deposited films exhibited a remarkable peak broadening that originates from a reduced crystallite size and/or microstrain. The reduction in the crystallite size and the increased microstrain could be caused by the collision of particles with the substrate during the AD process [8,41]. These XRD patterns were examined in detail using Rietveld refinements and the results are shown in Fig. 4b. As already mentioned, the starting HM30 powder shows intense and sharp reflections with a refined crystallite size of 181 nm ± 2 nm and a microstrain of $1.5\cdot10^{-4} \pm 0.1\cdot10^{-4}$. The as-deposited film has a reduced crystallite size of 33 nm ± 1 nm and an increased microstrain of $25.9\cdot10^{-4} \pm 0.3\cdot10^{-4}$, which developed in the films during the aerosol-deposition process. With further annealing at 500°C, the crystallite size does not change significantly and continues at around 38 nm ± 2 nm. On the other hand, annealing seems to reduce the microstrain by 47% (Fig. 4b).

To further investigate the residual stresses developed during the AD, a tilt-angle-dependent XRD analysis, i.e., the $\sin^2\Psi$ method

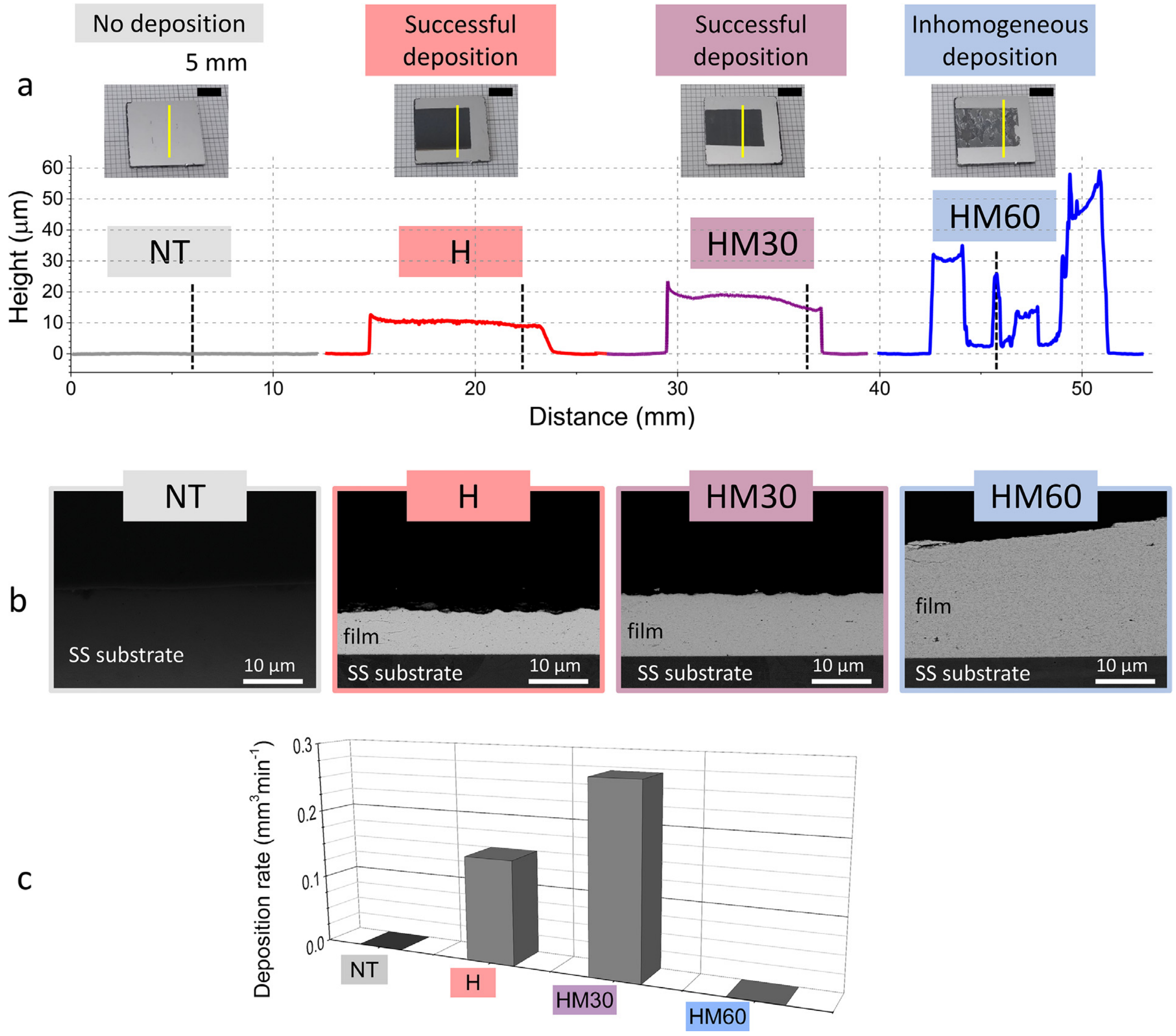

Fig. 3. (a) Photographs with the corresponding line profiles, (b) SEM cross-sectional images and (c) deposition rate of samples with differently modified powders. The measured line profiles are marked on the photographs with yellow lines. The estimated position of the SEM cross-sectional images is marked on the line profiles with black dashed lines. Note that the represented deposition rate of the HM60 powder is zero, due to the inhomogeneous film thickness. (For interpretation of the references to colour in this figure legend, the reader is referred to the web version of this article.)

[42], was performed on the as-deposited and annealed films. The (211) reflection was measured at different sample-tilting angles Ψ. The results shown in Fig. 4c reveal compressive in-plane residual stresses in the as-deposited films. The decrease in the slope indicates that the residual stresses partially relax when annealing the films, a result that is consistent with previous reports on AD thick films [19,43].

Additional stress analyses were performed using Raman spectroscopy. The Raman spectra of the as-deposited and annealed films are shown in Fig. 4d. The as-deposited film displays a slight peak shift towards higher wavenumbers. This is evident from the 270 cm^{-1} band, which is related to the mixed B-O-B-bending and O-B-O-stretching modes [44]. This mode is the only one influenced by temperature variations, and is expected to be sensitive to stress as well [45]. A shift towards higher wavenumbers in the as-deposited films can be associated with a higher compressive stress; recovery of this shift after annealing is thus compatible with a residual stress relaxation during annealing.

SEM images of as-deposited and annealed films are shown in Fig. 5a–d. The cross-sectional view of the as-deposited sample reveals a very dense film with excellent adhesion to the SS substrate (Fig. 5a). There is no apparent damaged layer at the film-substrate interface. The as-deposited film contains nm-sized pores that can be clearly distinguished at higher magnification, as shown in Supplementary material S3. In addition, the microstructure also reveals larger pores, a few tens of nm in size (Fig. 5a). Like the cross-sectional view (Fig. 5a), the surface-view (Fig. 5c) also reveals a very dense film. Excellent adhesion and high density were maintained after the annealing (Fig. 5b, d). Furthermore, no notable microstructural differences were observed between the as-deposited and the annealed films. In addition, the porosity of as-deposited and annealed films, which was estimated from SEM cross-sectional images, reached 1.6% and 1.5%, respectively. TEM images of the as-deposited films are shown in Fig. 5e, f. The SAED analyses of the film reveal its polycrystalline nature (inset of Fig. 5e). A clearly visible film-substrate interface in Fig. 5e confirms the excellent adhesion. The as-deposited film contains grains from 10 nm (Fig. 5f) to 200 nm in size (Fig. 5a, c, e).

Unipolar *P*–*E* hysteresis loops of the as-deposited and annealed films are shown in Fig. 6a. The as-deposited films exhibit a dielectric-like behavior at 300 kV·cm^{-1}. By increasing the electric field up to 900 kV·cm^{-1}, the *P*–*E* loop of the as-deposited film

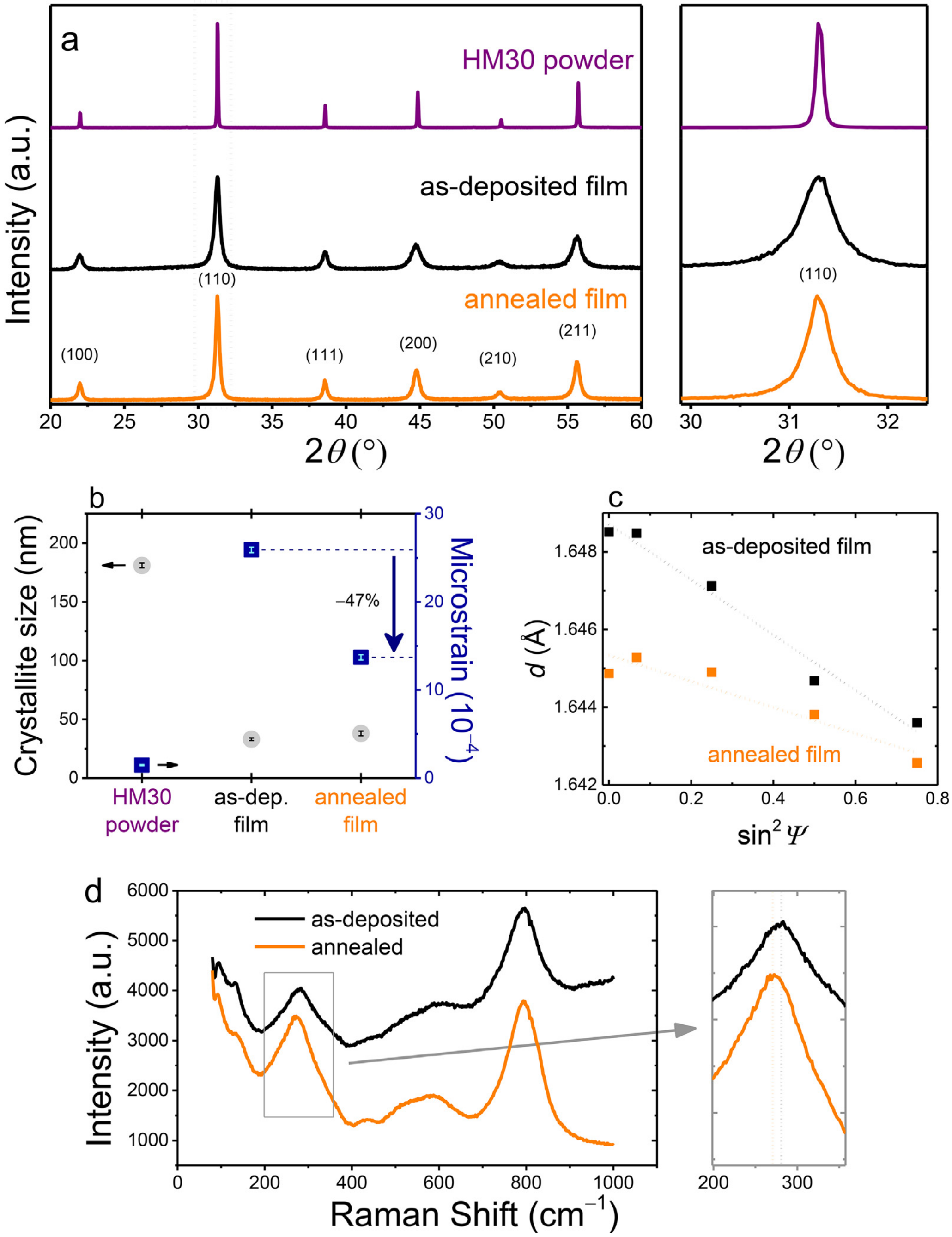

Fig. 4. (a) Zoom-in XRD patterns in the 2θ range 20–60° for HM30 powder and as-deposited and annealed films (left); enlarged view of (110) cubic reflection (right). (b) The corresponding crystallite size (grey circles) and microstrain (blue squares) evaluated using Rietveld refinement. (c) d-spacing of the (211) reflection plotted with respect to $\sin^2\Psi$ for as-deposited and annealed films. Dotted lines represent a linear fit to a measured data set. (d) Raman spectra of as-deposited and annealed thick films. The right panel shows an enlarged view of the 270 cm^{-1} peak. (For interpretation of the references to colour in this figure legend, the reader is referred to the web version of this article.)

opens slightly. By annealing the films at 500°C and thus partially releasing the stresses, the P–E loops develop a relaxor-ferroelectric character, reaching a maximum polarization (P_{max}) of 39 μC·cm^{-2} at 900 kV·cm^{-1}. Relaxor-like behavior is typical for PMN-rich compositions as well as for other PMN-PT compositions with the grain size in the range of hundreds of nm [46]. Such high polarization and low hysteresis losses make aerosol-deposited PMN–10PT films especially interesting for energy-storage applications.

In non-linear dielectrics, the recoverable energy density (U_{rec}) is calculated by integrating the area between the discharge curve and the polarization axis. An example of U_{rec} is shown by the orange patterned area in Fig. 6a. The charging-discharging of a ferroelectric-like capacitor is, in practice, associated with hysteresis, which represents the polarization losses. The energy-loss density (U_{loss}) is calculated by integrating the area between the charge and discharge curves. An example of U_{loss} is represented with the black patterned area in Fig. 6a. In addition to U_{rec}, the energy-storage efficiency (η) is an important parameter for evaluating the performance of materials used in energy-storage capacitors. η is defined as the ratio between the recovered and stored energy: $\eta = U_{rec}/(U_{rec}+U_{loss})$ [1].

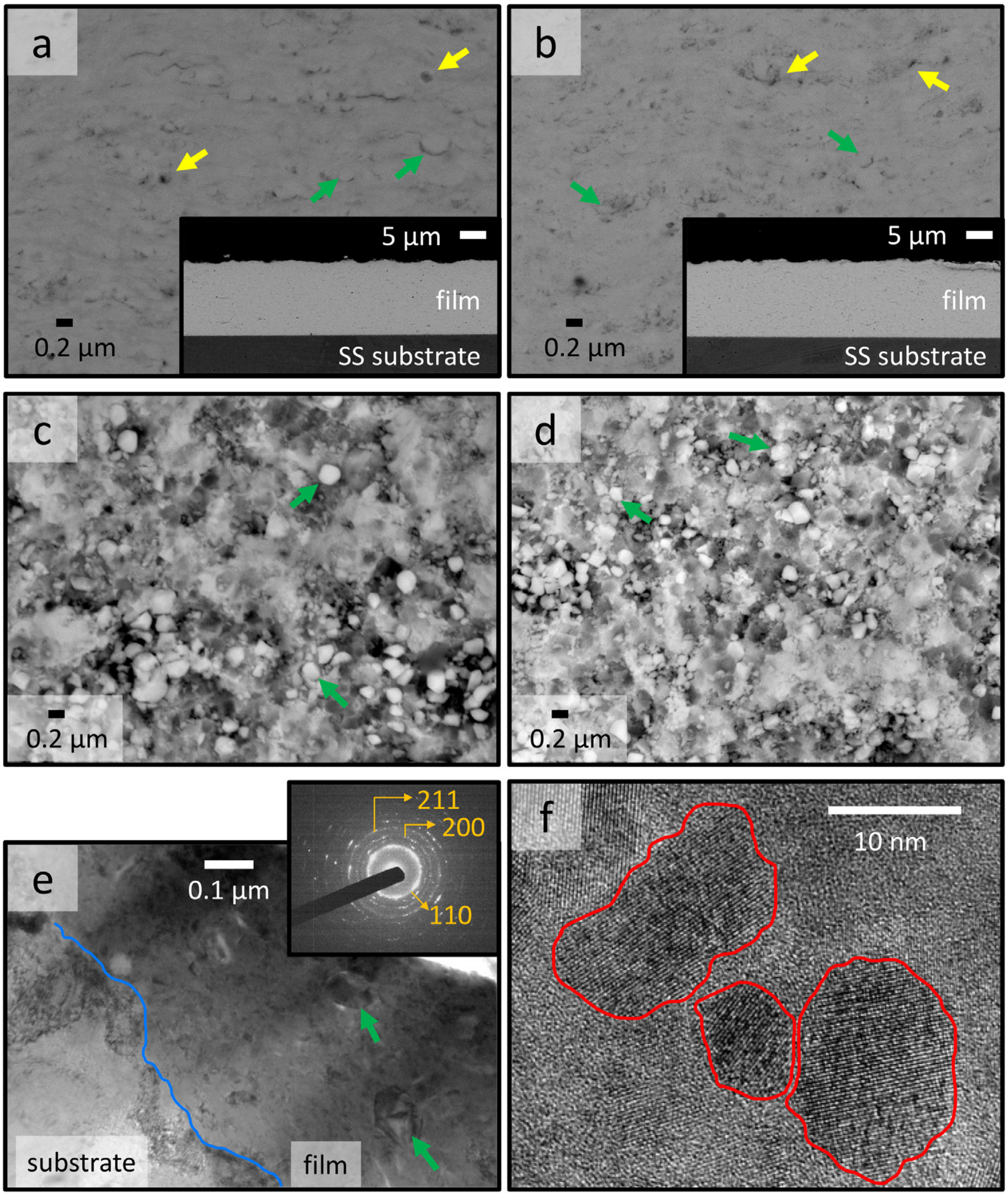

Fig. 5. SEM images of aerosol-deposited thick films (from the HM30 powder) in cross-section (a, b) and surface (c, d) views. SEM images represent as-deposited (a, c) and annealed (c, d) films. Bright-field TEM image (e) and high-resolution TEM image (f) of as-deposited thick film are shown in cross-sectional view. A SAED pattern of the film is shown in the inset (e). Pores, a few tens of nm large, and ~200-nm-large grains are marked with yellow and green arrows, respectively. The film-substrate interface and the grain boundaries are marked with blue and red lines, respectively. (For interpretation of the references to colour in this figure legend, the reader is referred to the web version of this article.)

The electric-field dependence of the energy-storage properties of the as-deposited and annealed films is shown in Fig. 6b. At low electric fields of 100 kV·cm^{-1}, the as-deposited and annealed films reach U_{rec} of 0.1 J·cm^{-3} and 0.4 J·cm^{-3}, respectively. These values are comparable with the U_{rec} values of PMN–10PT bulk ceramics that were prepared in our laboratory via mechanochemically assisted synthesis, followed by sintering (blue stars in Fig. 6b), as well as with the results of other reported aerosol-deposited thick films [47–49]. Furthermore, as-deposited and annealed films exhibit a similar η of ~85%, which is much higher than for bulk ceramics (~66%). The thickness of bulk ceramics is limited, typically down to few hundred µm, because of the mechanical thinning process. On the other hand, a-few-µm-thick films are ~100 times thinner than bulk ceramics and thus they require ~100-times-smaller applied voltages to reach the same electric field as the bulk ceramics.

U_{rec} shows a linear increase with the electric field, reaching a value of 7.0 J·cm^{-3} at 900 kV·cm^{-1} for the as-deposited films. This value is comparable to the aerosol-deposited PMN-based films [49] and magnetron sputtered PMN–10PT films [50], both deposited on conventional and costly Si substrates. Furthermore, the annealed films exhibit even higher U_{rec} values of 9.8 J·cm^{-3} at 900 kV·cm^{-1}. These results are comparable to other energy-storage-efficient AD thick films prepared on Si substrates [47-49,51,52] (Supplementary material S4). In comparison to screen-printed thick films [53] and bulk ceramics [54], the aerosol-deposited PMN–10PT thick films exhibit a significantly higher dielectric breakdown strength (DBS) and, consequently, a higher U_{rec}. Note that the dielectric breakdown of PMN–10PT bulk ceramics

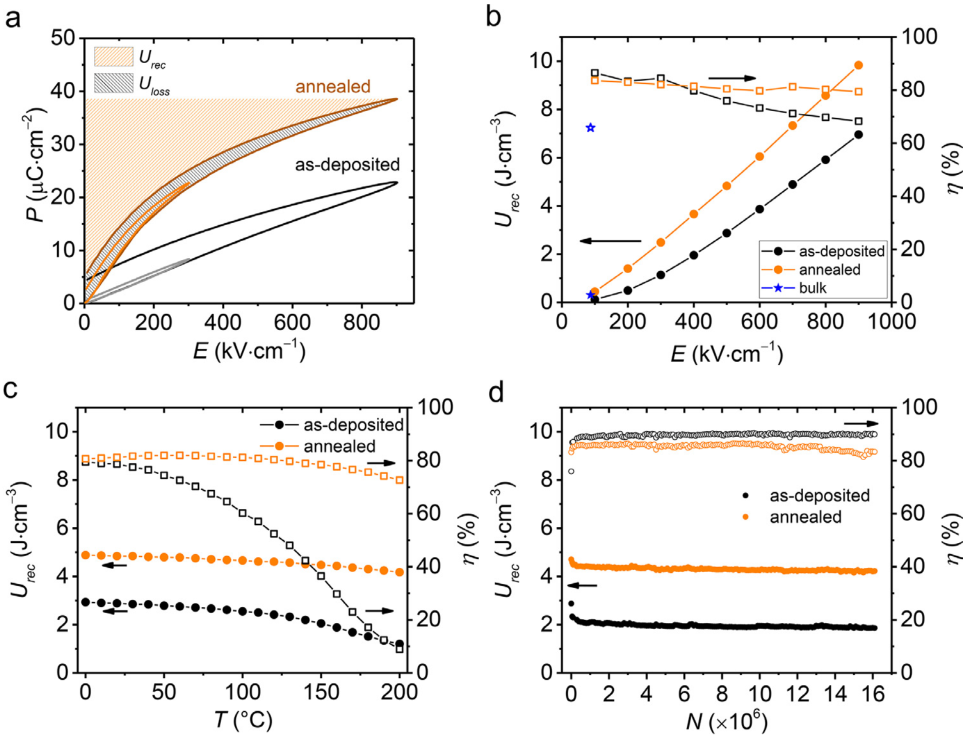

Fig. 6. (a) Unipolar P–E hysteresis loops of as-deposited and annealed thick films. Light- and dark-colored lines represent P–E loops measured up to 300 kV·cm^{-1} and 900 kV·cm^{-1}, respectively. The U_{rec} and U_{loss} of the annealed film are represented by the orange and black patterned areas, respectively. (b) The electric-field dependence of U_{rec} and η for the as-deposited and annealed thick films and the bulk ceramic. (c) The temperature dependence and (d) electric-field cycling dependence of U_{rec} and η for as-deposited and annealed thick films at 500 kV·cm^{-1}. Lines between the values are just a guide to the eye. (For interpretation of the references to colour in this figure legend, the reader is referred to the web version of this article.)

occurs already at ~100 kV·cm^{-1} (Fig. 6b). According to Weibull analysis, the DBS of as-deposited and annealed PMN-10PT thick films reaches 992 kV·cm^{-1} and 1106 kV·cm^{-1}, respectively (Supplementary material S5). The efficiency of energy-storage materials tends to decrease with the electric field [1]. In as-deposited films, η decreases from 87% at 100 kV·cm^{-1} to 68% at 900 kV·cm^{-1} ($\Delta\eta$ = 19%). On the other hand, the efficiency remains constant in annealed films, where η decreases from 84% at 100 kV·cm^{-1} to 79% at 900 kV·cm^{-1} ($\Delta\eta$ = 5%). The efficiency of our annealed thick films is similar to the most efficient PMN-based thick films deposited on Si substrates [49]. Additionally, a comparison of their stabilities, $\Delta\eta$, with an increasing electric field reveals the superior performance of our films.

The energy-storage properties of the as-deposited and annealed films at different temperatures and increasing numbers of electric-field cycles are shown in Fig. 6c and d, respectively. The U_{rec} and especially η of the as-deposited films decrease with increasing temperature. A reason for this decrease is related to the opening of the P–E hysteresis loops (Supplementary material S6), which is most probably associated with an increased electrical conductivity at elevated temperatures. At room temperature, sharp P–E loops are observed, while with increasing temperature, P–E loops become more rounded, indicating the presence of a leakage current. The increase in the electrical conductivity of the as-deposited films at elevated temperatures is evident from the increase in the dielectric losses *tan* δ (Supplementary material S7) and the local electrical current (Supplementary material S8) with increasing temperature. On the other hand, the annealed films exhibit sharp P–E loops even at elevated temperatures. These films also exhibit a sufficient temperature stability up to 200°C. Both the as-deposited and annealed films exhibit sufficient electric-field cycling stability until the occurrence of dielectric breakdown after 1.6·10^7 cycles (Fig. 6d).

4. Summary and conclusions

The room-temperature deposition of PMN–10PT thick films on low-cost stainless-steel substrates was investigated for the first time. Prior to the aerosol deposition, the properties of the PMN–10PT powder were optimized through heating and milling processes. A successful deposition of 15-μm-thick and very dense films on stainless-steel substrates was achieved with powder containing particles of a few hundreds of nanometres. The films exhibited excellent energy-storage properties already in the as-deposited forms, reaching 7.0 J·cm^{-3} of recoverable energy density and 68% of energy-storage efficiency at 900 kV·cm^{-1}.

The post-deposition thermal annealing of films at 500°C resulted in a significant stress relaxation of the deposited layers, which improved the U_{rec} and η, reaching 9.8 J·cm^{-3} and 79% at 900 kV·cm^{-1}, respectively. Furthermore, the excellent temperature stability of U_{rec} and η up to 200°C and the electric-field cycling stability up to 1.6·10^7 cycles make the films promising for energy-storage applications. To conclude, we successfully prepared energy-storage-efficient, 15-μm-thick films integrated directly onto more affordable stainless-steel substrates without any additional intermediate electrode layer, which opens up possibilities for new, integrated energy-storage applications. A low-cost AD method with a fast deposition rate has the potential to be used in mass production processes, which could significantly impact the availability and affordability of future electronic devices. Further research in the field of energy storage capacitors could target efficient lead-free materials [55] that are compatible with stainless-steel applications for everyday use, such as stainless-steel medical devices, smart buildings, vehicles and other stainless steel consumer products. Very promising groups of materials are antiferroelectrics and relaxor-antiferroelectrics, which combine relaxor and antiferroelectric properties [56–59].

Declaration of Competing Interest

The authors declare that they have no known competing financial interests or personal relationships that could have appeared to influence the work reported in this paper.

Acknowledgments

This work was funded by the Slovenian Research Agency (bilateral project BI-DE-20/21-012, young researcher project M. Sadl, research project N2-0212 and programme P2-0105) and Ultracool Directorś fund 2017. M. Deluca acknowledges funding from the European Research Council (ERC) under the European Union's Horizon 2020 research and innovation programme (grant agreement No 817190). U. Eckstein, N. H. Khansur, K. G. Webber acknowledge the financial support for their contributions to this work from the Deutsche Forschungsgemeinschaft under GRK2495/F as well as the travel support of the DAAD under project 57402168 as part of the PPP Slovenian Programme. N. H. Khansur acknowledges the financial support for this work from the Deutsche Forschungsgemeinschaft under grant No KH 471/2-1. The authors thank J. Cilenšek, S. Drnovšek and V. Fišinger for assistance in the laboratory.

Supplementary materials

Supplementary material associated with this article can be found, in the online version, at doi:10.1016/j.actamat.2021.117403.

References

[1] H. Palneedi, M. Peddigari, G.T. Hwang, D.Y. Jeong, J. Ryu, High-performance dielectric ceramic films for energy storage capacitors: progress and outlook, Adv. Funct. Mater. 28 (42) (2018) 1–33.

[2] V.K.Thakur Prateek, V.K. Thakur, R.K. Gupta, Recent progress on ferroelectric polymer-based nanocomposites for high energy density capacitors: synthesis, dielectric properties, and future aspects, Chem. Rev. 116 (7) (2016) 4260–4317.

[3] C.A. Randall, H. Ogihara, J.-R. Kim, G.-Y. Yang, C.S. Stringer, S. Trolier-McKinstry, M. Lanagan, High temperature and high energy density dielectric materials, in: 2009 IEEE Pulsed Power Conference, 2009, pp. 346–351.

[4] X. Hao, A review on the dielectric materials for high energy-storage application, J. Adv. Dielectr. 03 (01) (2013) 1330001.

[5] T.F. Zhang, X.G. Tang, Q.X. Liu, Y.P. Jiang, X.X. Huang, Q.F. Zhou, Energy-storage properties and high-temperature dielectric relaxation behaviors of relaxor ferroelectric $Pb(Mg_{1/3}\ Nb_{2/3})O_3–PbTiO_3$ ceramics, J. Phys. D. Appl. Phys. 49 (9) (2016) 095302.

[6] M. Kosec, D. Kuscer, J. Holc, Processing of ferroelectric ceramic thick films, Multifunctional Polycrystalline Ferroelectric Materials, Springer, Dordrecht, 2011.

[7] J. Akedo, Room temperature impact consolidation (RTIC) of fine ceramic powder by aerosol deposition method and applications to microdevices, J. Therm. Spray Technol. 17 (2) (2008) 181–198.

[8] D. Hanft, J. Exner, M. Schubert, T. Stöcker, P. Fuierer, R. Moos, An overview of the aerosol deposition method: process fundamentals and new trends in materials applications, J. Ceram. Sci. Technol. 6 (3) (2015) 147–181.

[9] A. Garner, Stainless Steels and Specialty Alloys for Pulp, and Biomass Conversion, Durham: Nickel institute, 2017 vol. 2.

[10] P. Snelgrove, Stainless steel automotive and transport developments, Int. Stainl. Steel Forum (2016) 1–5 [Online]. Available https://www.worldstainless.org/Files/issf/non-image-files/PDF/Stainlesssteelautomotiveandtransportdevelopments.pdf.

[11] G. Gedge, Structural uses of stainless steel - buildings and civil engineering, J. Constr. Steel Res. 64 (11) (2008) 1194–1198.

[12] J. Akedo, M. Lebedev, Effects of annealing and poling conditions on piezoelectric properties of $Pb(Zr_{0.52},Ti_{0.48})O_3$ thick films formed by aerosol deposition method, J. Cryst. Growth 235 (1–4) (2002) 415–420.

[13] J. Akedo, M. Lebedev, H. Sato, J. Park, High-speed optical microscanner driven with resonation of lam waves using $Pb(Zr,Ti)O_3$ thick films formed by aerosol deposition, Jpn. J. Appl. Phys. 44 (9B) (2005) 7072–7077.

[14] S.-C. Lin, W.-J. Wu, Fabrication of PZT MEMS energy harvester based on silicon and stainless-steel substrates utilizing an aerosol deposition method, J. Micromech. Microeng. 23 (12) (2013) 125028.

[15] Y. Kawakami, H. Yoshikawa, K. Komagata, J. Akedo, Powder preparation for 0.5 $Pb(Ni_{1/3}Nb_{2/3})O_3$-0.15 $PbZrO_3$-0.35$PbTiO_3$ thick films by the aerosol deposition method, J. Cryst. Growth 275 (1–2) (2005) 1295–1300.

[16] S. Baba, J. Akedo, Damage-free and short annealing of $Pb(Zr,Ti)O_3$ thick films directly deposited on stainless steel sheet by aerosol deposition with CO_2 laser radiation, J. Am. Ceram. Soc. 88 (6) (2005) 1407–1410.

[17] S.W. Oh, J. Akedo, J.H. Park, Y. Kawakami, Fabrication and evaluation of lead-free piezoelectric ceramic LF4 thick film deposited by aerosol deposition method, Jpn. J. Appl. Phys. 45 (9B) (2006) 7465–7470.

[18] Y. Kawakami, M. Watanabe, K.I. Arai, S. Sugimoto, Effects of substrate materials on piezoelectric properties of $BaTiO_3$ thick films deposited by aerosol deposition, Jpn. J. Appl. Phys. 55 (10) (2016) 10TA10.

[19] N.H. Khansur, U. Eckstein, L. Benker, U. Deisinger, B. Merle, K.G. Webber, Room temperature deposition of functional ceramic films on low-cost metal substrate, Ceram. Int. 44 (14) (2018) 16295–16301.

[20] J. Exner, M. Schubert, D. Hanft, J. Kita, R. Moos, How to treat powders for the room temperature aerosol deposition method to avoid porous, low strength ceramic films, J. Eur. Ceram. Soc. 39 (2–3) (2019) 592–600.

[21] R. Saunders, S.D. Johnson, D. Schwer, E.A. Patterson, H. Ryou, E.P. Gorzkowski, A self-consistent scheme for understanding particle impact and adhesion in the aerosol deposition process, J. Therm. Spray Technol. (2021).

[22] M. Schubert, J. Exner, R. Moos, Influence of carrier gas composition on the stress of Al_2O_3 coatings prepared by the aerosol deposition method, Materials 7 (8) (2014) 5633–5642.

[23] G. Han, J. Ryu, W.-H. Yoon, J.-J. Choi, B.-D. Hahn, J.-W. Kim, D.-S. Park, C.-W. Ahn, S. Priya, D.-Y. Jeong, Stress-controlled $Pb(Zr_{0.52}Ti_{0.48})O_3$ thick films by thermal expansion mismatch between substrate and $Pb(Zr_{0.52}Ti_{0.48})O_3$ film, J. Appl. Phys. 110 (12) (2011) 124101.

[24] J. Akedo, M. Lebedev, Microstructure and electrical properties of lead zirconate titanate ($Pb(Zr_{52}/Ti_{48})O_3$) thick films deposited by aerosol deposition method, Jpn. J. Appl. Phys. 38 (9B) (1999) 5397–5401.

[25] N.H. Khansur, U. Eckstein, K. Riess, A. Martin, J. Drnec, U. Deisinger, K.G. Webber, Synchrotron x-ray microdiffraction study of residual stresses in $BaTiO_3$ films deposited at room temperature by aerosol deposition, Scr. Mater. 157 (2018) 86–89.

[26] M. Dragomir, M. Otoničar, M. Vrabelj, L. Fulanović, S. Drnovšek, T. Rojac, B. Malič, Seeding effects on the mechanochemical synthesis of $0.9Pb(Mg_{1/3}Nb_{2/3})O_3–0.1PbTiO_3$, J. Eur. Ceram. Soc. 39 (5) (2019) 1837–1845.

[27] M. Vrabelj, H. Uršič, Z. Kutnjak, B. Rožič, S. Drnovšek, A. Benčan, V. Bobnar, L. Fulanović, B. Malič, Large electrocaloric effect in grain-size-engineered $0.9Pb(Mg_{1/3}Nb_{2/3})O_3$ $–0.1PbTiO_3$, J. Eur. Ceram. Soc. 36 (1) (2016) 75–80.

[28] M. Sadl, U. Tomc, U. Prah, H. Ursic, Protective Alumina coatings prepared by aerosol deposition on magnetocaloric gadolinium elements, Inf. MIDEM - J. Microelectron. Electron. Components Mater. 49 (3) (2019) 177–182.

[29] R.W. Cheary, A. Coelho, A fundamental parameters approach to X-ray line-profile fitting, J. Appl. Crystallogr. 25 (2) (1992) 109–121.

[30] H.P. Klug, L.E. Alexander, X-Ray Diffraction Procedures: For Polycrystalline and Amorphous Materials, 2nd Ed., John Wiley & Sons, New York, 1974.

[31] D. Balzar, N. Audebrand, M.R. Daymond, A. Fitch, A. Hewat, J.I. Langford, A.Le Bail, D. Louër, O. Masson, C.N. McCowan, N.C. Popa, P.W. Stephens, B.H. Toby, Size-strain line-broadening analysis of the ceria round-robin sample, J. Appl. Crystallogr. 37 (6) (2004) 911–924.

[32] D. Wilcox, B. Dove, B. McDavid, D. Greer, UTHSCSA Image Tool for Windows, Version 3.0, University of Texas Health Science Center, San Antonio, 2002.

[33] W.H. Walton, Feret's statistical diameter as a measure of particle size, Nature 162 (4113) (1948) 329–330.

[34] Microtrac Inc., "Microtrac S3500 particle size analyzer operation and maintenance manual," Largo, 2007.

[35] P. Baláž, et al., Hallmarks of mechanochemistry: from nanoparticles to technology, Chem. Soc. Rev. 42 (18) (2013) 7571–7637.

[36] P. Nieke, J. Kita, M. Häming, R. Moos, Manufacturing dense thick films of lunar regolith simulant EAC-1 at room temperature, Materials 12 (3) (2019) 487.

[37] D. Hanft, P. Glosse, S. Denneler, T. Berthold, M. Oomen, S. Kauffmann-Weiss, F. Weis, W. Häßler, B. Holzapfel, R. Moos, The aerosol deposition method: a modified aerosol generation unit to improve coating quality, Materials 11 (9) (2018) 5–6.

[38] J. Exner, M. Hahn, M. Schubert, D. Hanft, P. Fuierer, R. Moos, Powder requirements for aerosol deposition of alumina films, Adv. Powder Technol. 26 (4) (2015) 1143–1151.

[39] J. Akedo, M. Lebedev, Powder preparation in aerosol deposition method for lead zirconate titanate thick films, Jpn. J. Appl. Phys. 41 (11B) (2002) 6980–6984.

[40] K. Mihara, T. Hoshina, H. Takeda, T. Tsurumi, Controlling factors of film-thickness in improved aerosol deposition method, J. Ceram. Soc. Japan 117 (1368) (2009) 868–872.

[41] J. Akedo, Aerosol deposition of ceramic thick films at room temperature: densification mechanism of ceramic layers, J. Am. Ceram. Soc. 89 (6) (2006) 1834–1839.

[42] I.C. Noyan, T.C. Huang, B.R. York, Residual stress/strain analysis in thin films by X-ray diffraction, Crit. Rev. Solid State Mater. Sci. 20 (2) (1995) 125–177.

[43] M. Nakada, K. Ohashi, J. Akedo, Electro-optical properties and structures of $(Pb,La)(Zr,Ti)O_3$ and $PbTiO_3$ films prepared using aerosol deposition method, Jpn. J. Appl. Phys. 43 (9B) (2004) 6543–6548.

[44] A. Slodczyk, P. Daniel, A. Kania, Local phenomena of $(1-x)PbMg_{1/3}Nb_{2/3}O_3$-$xPbTiO_3$ single crystals ($0<x<0.38$) studied by Raman scattering, Phys. Rev. B 77 (18) (2008) 1–16.

[45] H. Idink, W.B. White, Raman spectroscopic study of order–disorder in lead magnesium niobate, J. Appl. Phys. 76 (3) (1994) 1789–1793.

[46] M. Algueró, J. Ricote, R. Jiménez, P. Ramos, J. Carreaud, B. Dkhil, J.M. Kiat, J. Holc, M. Kosec, Size effect in morphotropic phase boundary $Pb(Mg_{1/3}Nb_{2/3})O_3–PbTiO_3$, Appl. Phys. Lett. 91 (11) (2007) 112905.

[47] M. Peddigari, H. Palneedi, G.T. Hwang, K.W. Lim, G.Y. Kim, D.Y. Jeong, J. Ryu, Boosting the Recoverable Energy Density of Lead-Free Ferroelectric Ceramic Thick Films through Artificially Induced Quasi-Relaxor Behavior, ACS Appl. Mater. Interfaces 10 (24) (2018) 20720–20727.

[48] H.-B. Jung, J.-H. Lim, M. Peddigari, J. Ryu, D.H. Choi, D.-Y. Jeong, Enhancement of energy storage and thermal stability of relaxor $Pb_{0.92}La_{0.08}Zr_{0.52}Ti_{0.48}O_3$-$Bi(Zn_{0.66}Nb_{0.33})O_3$ thick films through aerosol deposition, J. Eur. Ceram. Soc. 40 (1) (2020) 63–70.

[49] C.K. Park, S.H. Lee, J.H. Lim, J. Ryu, D.H. Choi, D.Y. Jeong, Nano-size grains and high density of 65PMN-35PT thick film for high energy storage capacitor, Ceram. Int. 44 (16) (2018) 20111–20114.

[50] X. Wang, L. Zhang, X. Hao, S. An, High energy-storage performance of $0.9Pb(Mg_{1/3}Nb_{2/3})O_3$-$0.1PbTiO_3$ relaxor ferroelectric thin films prepared by RF magnetron sputtering, Mater. Res. Bull. 65 (2015) 73–79.

[51] S. Bin Kang, M.G. Choi, D.Y. Jeong, Y.M. Kong, J. Ryu, Energy storage properties of nano-grained antiferroelectric $(Pb, La)(Zr, Ti)O_3$ films by aerosol-deposition method, IEEE Trans. Dielectr. Electr. Insul. 22 (3) (2015) 1477–1482.

[52] A. Kumar, S.H. Kim, A. Thakre, G. Lee, Y.G. Chae, J. Ryu, Increased energy-storage density and superior electric field and thermally stable energy efficiency of aerosol-deposited relaxor $(Pb_{0.89}La_{0.11})(Zr_{0.70}Ti_{0.30})O_3$ Films, J. Therm. Spray Technol. 30 (3) (2020) 591–602.

[53] X. Hao, P. Wang, X. Zhang, J. Xu, Microstructure and energy-storage performance of $PbO–B_2O_3–SiO_2–ZnO$ glass added $(Pb_{0.97}La_{0.02})(Zr_{0.97}Ti_{0.03})O_3$ antiferroelectric thick films, Mater. Res. Bull. 48 (1) (2013) 84–88.

[54] P. Zhao, H. Wang, L. Wu, L. Chen, Z. Cai, L. Li, X. Wang, High-performance relaxor ferroelectric materials for energy storage applications, Adv. Energy Mater. 9 (17) (2019) 1803048.

[55] V. Veerapandiyan, F. Benes, T. Gindel, M. Deluca, Strategies to improve the energy storage properties of perovskite lead-free relaxor ferroelectrics: a review, Materials 13 (24) (2020) 1–47.

[56] P. Zhao, S. Wang, H. Tang, X. Jian, X. Zhao, Y. Yao, T. Tao, B. Liang, S.-G. Lu, Superior energy storage density and giant negative electrocaloric effects in $(Pb_{0.98}La_{0.02})(Zr, Sn)O_3$ antiferroelectric ceramics, Scr. Mater. 200 (2021) 113920.

[57] J. Li, Z. Shen, X. Chen, S. Yang, W. Zhou, M. Wang, L. Wang, Q. Kou, Y. Liu, Q. Li, Z. Xu, Y. Chang, S. Zhang, F. Li, Grain-orientation-engineered multilayer ceramic capacitors for energy storage applications, Nat. Mater. 19 (9) (2020) 999–1005.

[58] J. Li, F. Li, Z. Xu, S. Zhang, Multilayer lead-free ceramic capacitors with ultrahigh energy density and efficiency, Adv. Mater. 30 (32) (2018) 1802155.

[59] H. Wang, Y. Liu, T. Yang, S. Zhang, Ultrahigh energy-storage density in antiferroelectric ceramics with field-induced multiphase transitions, Adv. Funct. Mater. 29 (7) (2019) 1807321.